



Time series of the summertime diurnal variability in the atmospheric water vapour isotopic composition at Concordia station, East Antarctica

Inès Ollivier^{1,2*}, Thomas Lauwers^{2*}, Niels Dutrievoz², Cécile Agosta², Mathieu Casado², Elise Fourré²,
5 Christophe Genthon³, Olivier Jossoud², Frédéric Prié², Hans Christian Steen-Larsen¹, Amaëlle Landais²

¹Geophysical Institute, University of Bergen, and Bjerknes Centre for Climate Research, Bergen, Norway

²Laboratoire des Sciences du Climat et de l'Environnement, LSCE/IPSL, CEA-CNRS-UVSQ, Université Paris-Saclay, Gif sur Yvette, France

³Laboratoire de Météorologie Dynamique, LMD/IPSL, Sorbonne Université-CNRS, France

10 * These authors contributed equally to this work

Correspondence to: Inès Ollivier and Thomas Lauwers (ines.ollivier@uib.no, thomas.lauwers@lsce.ipsl.fr)

Abstract. Measurements of stable water isotopes in the atmospheric water vapour can be used to better understand the physical processes of the atmospheric water cycle. In polar regions, it is a key parameter to understand the link between the precipitation and snow isotopic compositions and interpret isotope climate records from ice cores. In this study we present a
15 novel 2.5-month record of the atmospheric water vapour isotopic composition during the austral summer 2023-2024 at Concordia Station (East Antarctica), from two independently calibrated laser spectrometers (CRDS and OF-CEAS measurement techniques) which are optimised to measure in low humidity environments. We show that both instruments accurately measure the summertime diurnal variability in the water vapour $\delta^{18}\text{O}$, δD , and d-excess when the water vapour mixing ratio is higher than 200 ppmv. We compare these measurements to the outputs of the isotope-enabled atmospheric
20 general circulation model LMDZ6-iso and show that the model exhibits biases in both the mean water vapour isotopic composition and the amplitude of the diurnal cycle, consistent with previous studies. Hence, this study provides a novel dataset of the atmospheric water vapour isotopic composition on the Antarctic Plateau, which can be used to evaluate isotope-enabled atmospheric general circulation models. The dataset is available on the public repository Zenodo (<https://doi.org/10.5281/zenodo.14569655>, Landais et al., 2024b).

25 1 Introduction

Stable water isotopes are unique tools to study the atmospheric water cycle, as they integrate information along successive phase changes. The relative abundances of the most common isotope species are expressed as $\delta^{18}\text{O}$ and δD values, in per mill (‰) (Craig, 1961). The second order parameter deuterium excess (d-excess = $\delta\text{D} - 8 \cdot \delta^{18}\text{O}$, Dansgaard, 1964), has been defined to capture kinetic fractionation during phase changes throughout the hydrological cycle.



30 In polar ice cores, $\delta^{18}\text{O}$ and δD have been traditionally interpreted as a temperature proxy based on empirical relationships
between the mean annual temperature and the isotopic composition of snow samples (e.g. Johnsen et al., 1992; Jouzel et al.,
2007; Lorius et al., 1979). Alongside, d-excess has been interpreted as a proxy for climatic conditions at the evaporative
source region (e.g. Landais et al., 2021; Stenni et al., 2010; Uemura et al., 2008; Vimeux et al., 1999). However, an
increasing number of studies have shown that this relationship between $\delta^{18}\text{O}$, δD , d-excess and climatic conditions is
35 affected by post-depositional processes at the ice sheet's surface (e.g. Casado et al., 2018, 2021; Ollivier et al., 2024; Steen-
Larsen et al., 2014; Town et al., 2024; Zuhr et al., 2023). Specifically, the atmospheric water vapor isotopic composition
above the ice sheet plays an important role on the isotopic signal found in the snow and firn through water vapor exchange
during sublimation and condensation cycles (Dietrich et al., 2023; Hughes et al., 2021; Madsen et al., 2019; Ritter et al.,
2016; Wahl et al., 2021, 2022).

40 Measurements of the atmospheric water vapour isotopic composition therefore provide key information on the processes at
play at the ice sheet's surface and the link between water isotope records in the snow and firn and climatic conditions. In
addition, such measurements can be used to evaluate the performances of isotope-enabled Atmospheric General Circulation
Models (isoAGCMs hereinafter) (e.g. Risi et al., 2010; Werner et al., 2011, Dutrievoz et al., *in review*) beyond the common
evaluation with surface snow samples that have been affected by post-depositional processes.

45 However, measuring the isotopic composition of water vapour in low humidity conditions below 500 ppmv, such as
encountered on the East Antarctic Plateau, is a technical challenge since most laser spectrometers are designed for measuring
accurately within a range of humidities between 5,000 and 30,000 ppmv. The vapour $\delta^{18}\text{O}$ and δD measured by laser
spectrometers strongly depends on humidity levels, which has to be taken into account for the calibration of the instruments
(Casado et al., 2016; Landais et al., 2024a; Leroy-Dos Santos et al., 2021; Steen-Larsen et al., 2013). This can lead to
50 corrections larger than the amplitude of the diurnal signal (Leroy-Dos Santos et al., 2021).

At Concordia Station, on the East Antarctic Plateau, previous measurements of the water vapour isotopic composition have
been limited in time (few weeks in December and early January, Casado et al., 2016, Leroy-Dos Santos et al., 2021) and
associated with uncertainties as large as 5 and 20‰ for $\delta^{18}\text{O}$ and δD , respectively, when the humidity was below 200 ppmv.
Therefore, there is a need to have measurements of the water vapour isotopic composition that are more accurate and over
55 longer time periods.

In this study, we present a time series of $\delta^{18}\text{O}$, δD and d-excess of the atmospheric water vapour at Concordia Station, with
an improved analytical precision compared to previous measurements. We installed two new laser spectrometers adapted for
low humidity measurements, together with a calibration unit also designed to generate low humidity levels (Leroy-Dos
Santos et al., 2021). The two analysers are based on different measurement techniques (Cavity Ring Down Spectroscopy -
60 CRDS - and Optical Feedback Cavity Enhanced Absorption Spectroscopy - OF-CEAS), which permits to compare both
instrumental techniques in the low humidity conditions at Dome C and evaluate the performance of the OF-CEAS
instrument, which has never been successfully measuring in the field at such low humidities. The thorough calibration of
both instruments permitted the production of a coherent and accurate 2.5-month long time series of the water vapour isotopic



composition at Concordia Station over the austral summer 2023-2024. We further use this novel dataset to compare with
65 outputs from the isoAGCM LMDZ6-iso, as an example on how the dataset can be used for model evaluation.

2 Methods and data

2.1 Instrumental set-up

Concordia station is located on the East Antarctic plateau in the vicinity of Dome C (75.10° S, 123.33° E) at an altitude of
3233 m above sea level and about 1000 km away from the coast. The site is characterised by a mean annual temperature of -
70 52°C (Genthon et al., 2021).

The instrumental set-up for the continuous analysis of the water vapour isotopic composition (Fig. 1) presented in this study
is installed in an underground “shelter”, a heated facility (+10°C) located 800 m upwind from the main station buildings
(75.10°S, 123.30°E). The setup is composed of (i) a heated sampling line, (ii) two laser spectrometers based on different
techniques optimised for water vapour isotope analysis at low humidities and (iii) a homemade low humidity generator to
75 perform automatic calibrations (LHLG, Leroy Dos Santos et al., 2021). The sampling line is a 16-meter long 1/4”
perfluoroalkoxy (PFA) line with an inlet situated about 50 cm above the snow surface (Fig. 1a). The line is insulated
and equipped with a heating cord to ensure a positive temperature and prevent condensation of water vapour. Water vapour
is pumped through the line with a typical flow of 10 L min⁻¹ and sent into the heated underground shelter, where the
calibrations and the measurements with both analysers are performed (Fig. 1b).

80

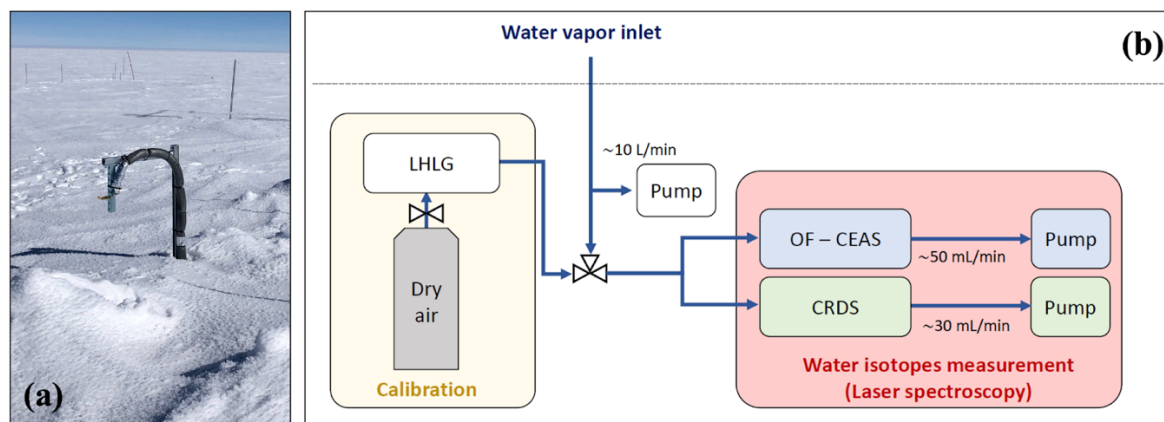


Figure 1: Schematic of the instrumental set-up for the continuous analysis of the water vapour isotopic composition at Dome C. Panel (a) shows a picture of the sampling line inlet above the snow surface. Panel (b) shows a schematic of the instrumental set-up with both analysers and the calibration unit (LHLG) inside the heated underground shelter.

85 The atmospheric water vapour isotopic composition is measured continuously in parallel by two distinct laser spectrometers,
respectively based on the CRDS technique and the OF-CEAS technique. The CRDS technique is based on an indirect
measurement of molecular absorption through the photon lifetime measurement inside a highly reflective resonant cavity.



The OF-CEAS measurement technique also relies on an optical cavity to increase the signal to noise ratio but directly measures the transmitted light. In addition, this technique uses optical feedback to stabilise the laser emission frequency, enabling a lower instantaneous noise compared to the CRDS technique.

A CRDS analyser, manufactured by Picarro company (Picarro analyser hereinafter), was first installed in the summer season 2014-2015 for a test season and a new analyser was installed permanently in 2018 at Concordia station (Picarro HIDS2319). These instruments, coupled to the calibration unit, have proven to be robust and adapted for field measurements (Casado et al., 2016; Leroy-Dos Santos et al., 2021). However, increasing uncertainties on the signal below 300 ppmv led to restrict the studies to December and January at Concordia station. Due to instrumental issues, the Picarro analyser HIDS2319 was replaced during the summer season 2021-2022 by a new analyser (Picarro HIDS2308 hereafter). The data presented in this study were collected by the latter. In parallel to the Picarro analyser, an OF-CEAS analyser manufactured by AP2E company (AP2E analyser hereinafter, Lauwers et al., 2024) was installed during the summer season 2022-2023 and optimised during the summer season 2023-2024. In this study we focus on the most recent austral summer period 2023-2024 (December to mid-March), where both AP2E and Picarro analysers have been optimised and measuring in parallel on site.

2.2 Calibration protocols

In order to produce accurate atmospheric water vapour content and isotope measurements, we perform a series of calibration steps on the data provided by the two laser spectrometers. The mixing ratios measured by both instruments are calibrated against independent humidity measurements (Sect. 2.2.1). The raw isotopic ratios are corrected for the isotope-humidity dependence of both analysers (Sect. 2.2.2) and then calibrated against the VSMOW-SLAP scale (Sect. 2.2.3). Lastly, section 2.2.4 presents the uncertainty estimation of the final calibrated measurements.

2.2.1 Calibration of the water vapour mixing ratio

To evaluate the accuracy of the measurement and calibrate the humidity measured by both analysers, we compare it to an independent in-situ measurement of the atmospheric humidity between January and March 2024. Note that data from this independent measurement was not available in December 2023, so the comparison is restricted to the beginning of 2024 although the analysers were operating in December 2023.

The independent humidity sensor is installed about two meters above the surface and about twenty meters away from the inlet of the laser spectrometers. The sensor is an adapted HMP155 sensor, specifically designed to accurately measure the atmospheric humidity in dry and cold environments with frequent supersaturation conditions (Genthon et al., 2017, 2022). As in Genthon et al. (2017), Vignon et al. (2022) and Ollivier et al. (2024), we use the data from the adapted HMP155 to recalculate the relative humidity with respect to ice. The relative humidity with respect to ice is then converted to water vapour mixing ratio (in ppmv) using the equations from Murphy and Koop (2005) together with the air pressure given by ERA5. Note that the resulting water vapour mixing ratio is not sensitive to the possible mismatch between the pressure given



120 by ERA5 and the local atmospheric pressure (not shown). We use this independent humidity measurement as the true atmospheric humidity content to correct the humidity measured by the Picarro and AP2E analysers, as follows:

$$hum_{corr} = hum_{meas} \cdot slope_{hum} + int_{hum} \quad (1)$$

125 Where hum_{meas} is the raw humidity given by the analyser (either AP2E or Picarro), hum_{corr} is the humidity corrected on the independent measurement and the coefficients $slope_{hum}$ and int_{hum} are determined by a linear regression between the hum_{meas} and the independent humidity measurement. The results of the linear regressions are presented in Sect. 3.1.1.

2.2.2 Influence of humidity on the measured isotopic ratios

130 For continuous water vapour isotopic measurement, and in particular in the East Antarctic plateau where mixing ratios are often below 500 ppmv, both OF-CEAS and CRDS techniques are affected by the dependency of isotopic measurements on the water vapour mixing ratio (e.g. Lauwers et al., 2024; Weng et al., 2020). We refer to this effect as the humidity-isotope response. This humidity-isotope response is instrument-specific (e.g. Steen-Larsen et al., 2013) and is dependent on the isotopic composition of the laboratory standard used to perform the calibrations (e.g. Lauwers et al., 2024; Weng et al., 2020). A calibration of this dependency is therefore required in the humidity range of the site and using laboratory standards with a known isotopic composition close to what is observed on site.

135 We determined the humidity-isotope response curves by performing one series of calibrations in January 2024. The calibration curves for both analysers are determined using a single custom laboratory standard (FP5, $\delta^{18}O = -50.52 \pm 0.05\%$ and $\delta D = -394.7 \pm 0.7\%$), calibrated against the VSMOW-SLAP scale. We assume that the humidity-isotope response of both analysers (AP2E and Picarro) is stable in the range of isotopic values measured on site, which was validated for a Picarro analyser in Leroy Dos Santos et al. (2021). The standard FP5 has an isotopic composition closest to the water vapour isotopic composition measured on site (from -50 to -80‰ in $\delta^{18}O$ and from -550 to -400‰ in δD during summer months and it has been previously used to calibrate a Picarro laser spectrometer at the same site (Leroy-Dos Santos et al., 2021). The calibration steps were performed from high to low humidity (humidities ranging from 1100 to 50 ppmv). The humidity levels are generated using the newest version of the custom calibration unit (LHLG, Leroy-Dos Santos et al., 2021), which enables the generation of a steady water vapour flux with a known and stable isotopic composition.

145 The reference humidity for the calibration curves is set to 500 ppmv (see also Sect. 2.2.3). The results of the different calibration steps are fitted with inverse functions (in combination to a linear function), as done in previous studies (e.g. Lauwers et al., 2024). The coefficients of the inverse fits are used to correct the raw isotope data for the humidity-isotope response, as follows:

$$150 \quad \delta_{i,humcorr} = \delta_{i,meas} - \left[\frac{1}{c_1} \cdot hum_{meas} + c_2 \cdot hum_{meas} + c_3 \right] \quad (2)$$



Where $\delta_{i,\text{meas}}$ is the raw isotope data given by the instruments (subscript i is for any isotope species, $\delta^{18}\text{O}$ or δD), $\delta_{i,\text{humcorr}}$ is the isotope data corrected for the humidity-isotope response of the instruments and the coefficients c_1 , c_2 , and c_3 correspond to the coefficients of the inverse functions fitted to the data of the calibration steps. Equation 2 is determined for each isotope species and each analyser. The results of the calibration steps, the inverse fits and the coefficients are presented in Sect. 3.1.2.

2.2.3 Absolute calibration of the measured isotopic ratios

In a second step, we perform the absolute calibration of both analysers to convert the raw isotopic compositions measured by the instruments (and corrected for humidity dependence beforehand) to isotopic values calibrated against the VSMOW-SLAP scale. Regular and automatic calibrations of both analysers are performed with two laboratory standards calibrated against VSMOW-SLAP (FP5: $\delta^{18}\text{O} = -50.52\text{‰}$ and $\delta\text{D} = -394.7\text{‰}$; NEEM: $\delta^{18}\text{O} = -33.5\text{‰}$ and $\delta\text{D} = -257.2\text{‰}$). The calibrations are performed every 48 to 72 hours with the LHLG, injecting both standards at a target humidity level of 500 ppmv. We use the isotopic ratios measured by both analysers during the calibrations between January 11th and June 6th 2024 to establish the linear equations for the absolute calibration of each instrument. To remove the influence of the humidity measured during each calibration on the measured isotopic ratios during the calibration step, we correct the isotopic ratios for the humidity-isotope dependence (Sect. 2.2.2). In addition, we discard the calibrations with a humidity outside of two standard deviations around the mean humidity and outside of two standard deviations around the mean isotopic ratio of all calibrations during the period. Because we do not observe any significant drift in the calibration data, we then average, for each laboratory standard and each analyser, the measured water isotopic composition of all the selected calibrations over the period and establish the linear equations against the true value of the standards. The linear functions for each analyser are used to calibrate the measurements against the VSMOW-SLAP scale, as follows:

$$\delta_{i,\text{VSMOW-SLAP}} = \delta_{i,\text{humcorr}} \cdot \text{slope}_{\text{VSMOW-SLAP}} + \text{int}_{\text{VSMOW-SLAP}} \quad (3)$$

Where $\delta_{i,\text{humcorr}}$ is the isotope data corrected for humidity-isotope response (subscript i is for any isotope species, $\delta^{18}\text{O}$ or δD , see Sect. 2.2.2 and Eq. 2), $\delta_{i,\text{VSMOW-SLAP}}$ is the final corrected and calibrated against VSMOW-SLAP isotope data and the coefficients $\text{slope}_{\text{VSMOW-SLAP}}$ and $\text{int}_{\text{VSMOW-SLAP}}$ are determined by the linear regression between the measured and true values of the two laboratory standards. The results of the absolute calibration step are presented in Sect. 3.1.3. The corrected and calibrated time series of the water vapor isotopic composition from both analysers are presented in Sect. 3.2.

It should be noted that the two laboratory standards used to perform the absolute calibration both have an isotopic composition above the one usually measured on site in the atmosphere. We therefore assume that the linear relationships between the true and measured $\delta^{18}\text{O}$ and δD values can be extrapolated beyond the isotopic composition of both standards to be able to calibrate the in-situ measurements. Such assumption was validated for a Picarro analyser in Casado et al. (2016).



2.2.4 Estimation of measurement uncertainty

185 We present two approaches to estimate the uncertainty on the water vapour isotopic measurements. First, we propagate the uncertainty related to the measurement noise driven by low humidity measurements and day-to-day instrumental drift, which is manifested in the regular measurements of the two laboratory standards. Secondly, we carry out a Monte-Carlo simulation propagating the uncertainty of the absolute calibration against VSMOW-SLAP into the uncertainty estimate on the final calibrated water vapour isotope measurements.

190 We consider two sources of uncertainty associated with the $\delta^{18}\text{O}$ and δD measurements. The first source of uncertainty follows a power law with respect to humidity due to the increase in measurement noise at lower humidity levels for both Picarro and AP2E analysers (Lauwers et al., 2024). The second uncertainty originates from the instrumental instabilities at hourly to daily time scales caused by the sensitivity of the optical signal of laser spectrometers to several environmental factors, such as temperature or mechanical perturbations. We refer to the latter uncertainty as the “drift” uncertainty. We
195 group the two uncertainties (noise at low humidity and drift) into the following formulation to estimate the combined uncertainty on $\delta^{18}\text{O}$ and δD measurements:

$$\sigma_i(h) = (\sigma_{i,\text{drift}} \cdot h_{\text{ref}}) / h \quad (4)$$

200 With h_{ref} is the reference humidity of the calibration steps ($h_{\text{ref}} = 500$ ppmv, Sect. 2.2.2 and 2.2.3) and h is the humidity measured by the laser spectrometers. $\sigma_{i,\text{drift}}$ corresponds to one standard deviation of the measured isotopic ratios (subscript i is for any isotope species, $\delta^{18}\text{O}$ or δD) of all the calibration steps performed over six months with two laboratory standards (selected calibrations steps, see Sect. 2.2.3).

The uncertainty is calculated for the whole dataset for both analysers and is valid from 50 to 1100 ppmv (i.e. corresponding
205 to the upper and lower limit of the humidity-response curves, see Sect. 2.2.2). With this method, the uncertainty on the data incorporates both the instrumental drift over six months, similarly as done by Casado et al. (2016), and the dependency of the uncertainty on the measured humidity (i.e. larger uncertainties at lower humidities). This measurement uncertainty is probably overestimated, as $\sigma_{i,\text{drift}}$ integrates both the drift from the LHLG and from each isotope analyser over a six-month period. The uncertainty $\sigma(h)$ for d-excess is calculated by propagating the uncertainties on $\delta^{18}\text{O}$ and δD , as follows:

210

$$\sigma_{d-\text{excess}}(h) = \sqrt{\sigma_{\delta\text{D}}(h)^2 + \sigma_{\delta^{18}\text{O}}(h)^2} \quad (5)$$

Alternatively, we propose to compute the uncertainty on the final $\delta^{18}\text{O}$ and δD values from the Picarro and AP2E analysers by performing a Monte Carlo test with 1000 resamples of the linear regression coefficients within their uncertainty range to
215 calibrate the $\delta^{18}\text{O}$ and δD values against the VSMOW-SLAP scale (as described in Sect. 2.2.3 but including uncertainty on the linear equation coefficients in Eq. 3). The uncertainty (referred as σ_{MC}) is computed as one standard deviation of the 1000



Monte Carlo calibrated time series and should be similar to σ_{drift} , since the same dataset of calibration steps is used for both methods. We compute the uncertainty for d-excess by propagating the uncertainties on $\delta^{18}\text{O}$ and δD , using Eq. 5. Results of this analysis are presented in Sect. 3.1.4.

220 2.3 Model description

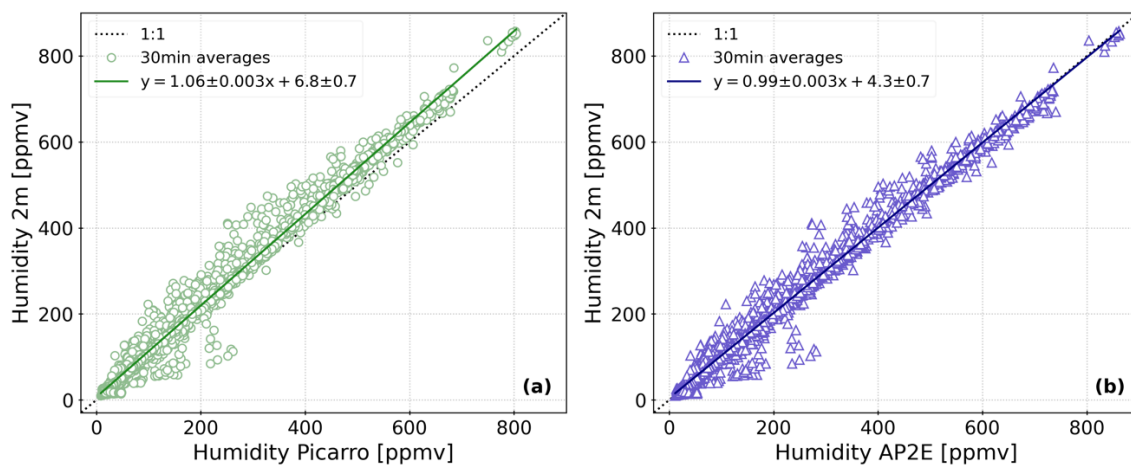
The LMDZ-iso model (Laboratoire de Météorologie Dynamique Zoom model equipped with water isotopes, Risi et al., 2010) is the isotopic version of the atmospheric general circulation model LMDZ6 (Hourdin et al., 2020). The version of LMDZ used here is nearly identical to the one used for the phase 6 of the Coupled Model Intercomparison Project (CMIP6, Eyring et al., 2016). The LMDZ6 model employs the Van Leer moisture advection scheme for the passive transport of water isotopes (Risi et al., 2010; Van Leer, 1977). The equilibrium fractionation coefficients between water vapour and liquid or ice phases are derived from Merlivat and Nief (1967) and Majoube (1971a, 1971b). The non-equilibrium (kinetic) fractionation coefficients are formulated by Merlivat and Jouzel (1979) for evaporation from the sea surface and by Jouzel and Merlivat (1984) for snow formation at supersaturation. We performed a simulation with the standard Low Resolution (LR) grid of LMDZ6 with a horizontal resolution of 2.0° in longitude and 1.67° in latitude (144×142 longitude-latitude grid). The simulation has 79 vertical levels, and the first atmospheric level is located around 10 m above ground level. The LMDZ-iso 3D-fields of temperature and wind are nudged toward the 6-hourly ERA5 reanalysis data with a relaxation time of 3 hours except below the sigma-pressure level corresponding to 850 hPa above sea level, where nudging is not applied. Surface ocean boundary conditions are taken from the monthly mean sea surface temperature and sea-ice concentration fields from the ERA5 reanalysis. The simulation is performed with a supersaturation parameter of 0.004 K^{-1} . The simulation covers the period from December 2023 to April 2024, with a 1-hourly resolution.

3 Results

3.1 Dataset calibration

3.1.1 Water vapour mixing ratio

Figure 2 shows the evaluation of the atmospheric mixing ratio (or humidity, in ppmv) measured by the two analysers (Picarro and AP2E) against an independent humidity sensor (Sect. 2.2.1). The humidity measured by both analysers agree very well with the independent humidity measurement, with linear regression slopes close to the one-to-one line for both analysers (Fig. 2a and b). Overall, the Picarro analyser measures a lower humidity content than the independent sensor (average difference of 20 ppmv between January 1st and March 15th 2024), especially at higher humidity levels (Fig. 2a). On the other hand, the AP2E analyser gives similar humidities than the independent sensor (average difference of 2 ppmv between January 1st and March 15th 2024) in the whole range of humidities (Fig. 2b).



250 **Figure 2: Humidity (ppmv) measured by the two laser spectrometers (Picarro in panel (a) and AP2E in panel (b)) versus humidity measured by the independent sensor (modified HMP155, Sect. 2.2.1). All available 30 min averages between January 1st and March 15th 2024 are shown in the figure.**

Even if the difference between the humidity measured by the Picarro and AP2E analysers and the independent humidity sensor is small, the linear regression coefficients $\text{slope}_{\text{hum}}$ and intercepts at origin int_{hum} (Fig. 2, Table 1) can be used to calibrate the humidity measured by both analysers, as described in Section 2.2.1.

255 **Table 1. Linear regression coefficients (shown in Fig. 2 and used in Eq. 1) for the correction of the humidity measured by both the Picarro and AP2E analysers.**

	$\text{slope}_{\text{hum}}$ [ppmv ppmv ⁻¹]	int_{hum} [ppmv]
Picarro HIDS2308	1.06	6.8
AP2E	0.99	4.3

260

During the period of interest (December 2023 to March 15th 2024), the humidity measured and calibrated by the two laser spectrometers ranges from 15 to 1100 ppmv (see also Fig. 6, Sect. 3.2). Note that the lowest humidity measured by the modified HMP155 system during this period is about 1 ppmv, however the two laser spectrometers didn't record this low humidity due to gaps in the dataset (Sect. 3.2).

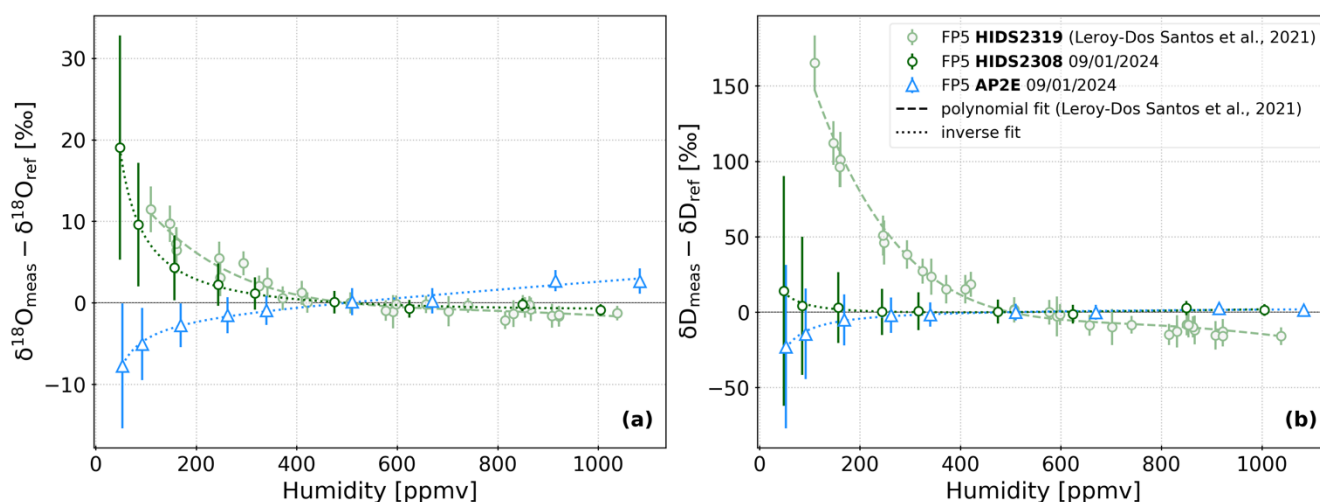
265 3.1.2 Humidity-isotope response

Figure 3 shows the humidity-isotope calibration curves determined with the laboratory standard FP5 ($\delta^{18}\text{O} = -50.52\%$ and $\delta\text{D} = -394.7\%$, Sect. 2.2.2), for three laser spectrometers (described in Sect. 2.1): (1) the Picarro HIDS2319 analyser from Leroy-Dos Santos et al. (2021), (2) the Picarro HIDS2308 analyser (this study) and (3) the AP2E analyser (this study). For the Picarro HIDS2319 analyser, the calibration steps were performed with the initial version of the LHLG while for this study (Picarro HIDS2308 and AP2E analysers), the calibration steps were performed with the newest version of the LHLG

270



(Sect. 2.2.2). Each point on the humidity-response curves of all three analysers corresponds to the average isotopic composition of the calibration step over a ten-minute stable period. Note that each calibration step lasted from 40 min to 1h. In Leroy-Dos Santos et al. (2021), the humidity-isotope response curves (for both $\delta^{18}\text{O}$ and δD) of the Picarro HIDS2319 are described with polynomial fits (their equations 4 and 5, light green dashed lines in Fig. 3a and b). Their results show a divergence of the measured isotopic composition below 500 ppmv, especially strong for δD (light green dashed line and dots in Fig. 3b). For the Picarro analyser HIDS2308, the humidity-isotope response curves are described with inverse fits (Sect. 2.2.2, dark green dotted lines in Fig. 3a and b). In comparison to the HIDS2319 analyser, the response curves show a similar strong divergence in $\delta^{18}\text{O}$ and a much weaker divergence in δD . In addition, the HIDS2308 curves don't show any humidity-isotope dependence above 500 ppmv for both $\delta^{18}\text{O}$ and δD (dark green dotted lines and dots in Fig. 3a and b). The difference in humidity-isotope response of the two Picarro analysers (HIDS2319 and HIDS2308) is not surprising since different spectrometers will have a different humidity-isotope response (e.g. Steen-Larsen et al., 2013). For the AP2E analyser, the humidity-isotope response curves are also described with inverse fits (Sect. 2.2.2, blue dotted lines in Fig. 3a and b). As already identified and described in Lauwers et al. (2024), the AP2E analyser humidity-isotope response curves show two different regimes. Below 500 ppmv, both $\delta^{18}\text{O}$ and δD show a divergence with decreasing humidity levels, in the opposite direction as for both Picarro analysers (blue dotted lines in Fig. 3a and b). Above 500 ppmv, $\delta^{18}\text{O}$ shows a positive linear dependency to increasing humidity (blue dotted line in Fig. 3a), while a weaker dependency is observed for δD (blue dotted line in Fig. 3b).



290 **Figure 3: Humidity-isotope ($\delta^{18}\text{O}$ in panel (a) and δD in panel (b)) response curves for both the Picarro HIDS2319 (Leroy-Dos Santos et al., 2021), and the two laser spectrometers used in this study (Picarro HIDS2308 and AP2E analysers). The calibration steps and the data fitting are described in Sect. 2.2.2. In both panels, the dashed and dotted lines represent respectively a polynomial and inverse fit on the data. The error bars show the standard deviation around the 10-min average period of each calibration step of the three analysers (1σ , i.e. representation of the measurement noise). Note that to have the same reference humidity (500 ppmv) for all three calibrations curves, the curves for the Picarro HIDS2319 were shifted downwards by the isotopic values of the polynomial fit at 500 ppmv (reference initially measured at 2000 ppmv, Leroy-Dos Santos et al., 2021).**



These results show that the isotope-humidity response of the Picarro analyser presented in this study is better constrained compared to the previous Picarro analyser, with a calibration curve determined down to a lower humidity than in Leroy-Dos Santos (50 ppmv in this study, 110 ppmv previously). In addition, the new Picarro shows a weaker isotope-humidity dependence in the range of observed humidities at Dome C over the period of interest (15 to 1100 ppmv, Sect. 3.1.1), which leads to a better constrain on the correction for the isotope-humidity response and improves the reliability of the dataset. These results also show a well constrained isotope-humidity dependence for the AP2E analyser in the range of observed humidities at Dome C over the period of interest, which similarly to the Picarro analyser, improves the reliability of the dataset.

It should still be noted that the isotope-humidity calibration only goes down to 50 ppmv, although the minimum humidity recorded by the instruments is 15 ppmv during the period of interest (and the overall minimum humidity recorded by the HMP155 is 1 ppmv, Sect. 3.1.1). To correct the dataset, we therefore extrapolate the calibration curve down to 15 ppmv. This can lead to abnormal isotopic values after correction, leading to the increase of the uncertainty on the data at low humidities. This point is further developed in Sect. 3.1.4.

Table 2 summarises the coefficients of the inverse fits shown in Fig. 3 for both the Picarro HIDS2308 and AP2E analysers. As described in Sect. 2.2.2, these coefficients are used in Eq. 2 to calibrate the isotope measurements from both analysers for the humidity-isotope dependence (following Eq. 2, positive values in Fig. 3 correspond to a negative correction).

Table 2. Coefficients of inverse functions (shown in Fig. 3 and used in Eq. 2) to calibrate the instruments for the humidity-isotope response of both the Picarro and AP2E analysers.

	$\delta^{18}\text{O}$			δD		
	C_1 [ppmv]	C_2 [ppmv ⁻¹]	C_3 [ppmv ppmv ⁻¹]	C_1 [ppmv]	C_2 [ppmv ⁻¹]	C_3 [ppmv ppmv ⁻¹]
Picarro HIDS2308	1024.9	0.0007	-2.4	822.1	0.005	-4.3
AP2E	-336.2	0.005	-1.6	-1414.7	0.0005	2.6

3.1.3 Absolute calibration of isotopic ratios

As described in Sect. 2.2.3, the absolute calibration against the VSMOW-SLAP scale of the isotope data given by the Picarro and the AP2E analysers relies on the results of regular calibrations over six months of two laboratory standards with known isotopic composition. Figure 4 shows the results of these regular calibrations performed between January and June 2024.

We first see that, despite a target humidity of 500 ppmv, the humidity measured during these regular calibrations varies slightly, from 250 to 450 ppmv, depending on which instrument and standard is measured (Fig. 4a). We also see that some of the calibrations are associated with very low humidities (red markers in Fig. 4a), which we exclude in the pool of calibrations used for the absolute calibration of both analysers (Sect. 2.2.3). These low humidity calibrations can be explained by the LHLG, which failed to generate the target humidity level.

We observe that the measured $\delta^{18}\text{O}$ by both analysers varies throughout the period, but no drift is observed (Fig. 4b). Since the $\delta^{18}\text{O}$ values shown in Fig. 4b are corrected for the humidity-isotope response (Sect. 2.2.3), variations around the mean



$\delta^{18}\text{O}$ over the whole period cannot be explained by the variations of the humidity measured by the analysers (Fig. 4a). Instead, these variations can be explained by variations of environmental conditions, such as the temperature in the room where the spectrometers are installed, or instability of the humidity generated by the LHLG during the calibration step. Despite these variations, the standard deviation of the ensemble of $\delta^{18}\text{O}$ values associated to the calibration of the two laboratory standards is low for both instruments (1.0‰ for the standard NEEM measured by the AP2E analyser and 0.8‰ for FP5; 0.8‰ for the standard NEEM measured by the Picarro analyser and 0.6‰ for FP5; Fig. 4b) compared to results from Lauwers et al. (2024) obtained at Dumont d'Urville station over a year. We further exclude the few calibrations which appear as outliers (outside of two standard deviations around the mean $\delta^{18}\text{O}$, red markers in Fig. 4b) to establish the absolute calibration of both analysers (Sect. 2.2.3).

As for $\delta^{18}\text{O}$, we do not observe any drift in δD over the period, for neither analyser (Fig. 4c). The standard deviation of the ensemble of δD values associated with the calibration of the two laboratory standards is low for both instruments (7.4‰ for the standard NEEM measured by the AP2E analyser and 6.5‰ for FP5; 6.9‰ for the NEEM standard measured by the Picarro analyser and 2.4‰ for FP5; Fig. 4c). These results are comparable with the results from Lauwers et al. (2024). For both laboratory standards, the variations in δD over the period are higher for the AP2E analyser, which is probably due to the small absorption peak of δD in the spectral window used by the analyser. We further exclude the few calibrations which appear as outliers (outside of two standard deviations around the mean δD , red markers in Fig. 4c) to establish the absolute calibration of both analysers (Sect. 2.2.3).

345

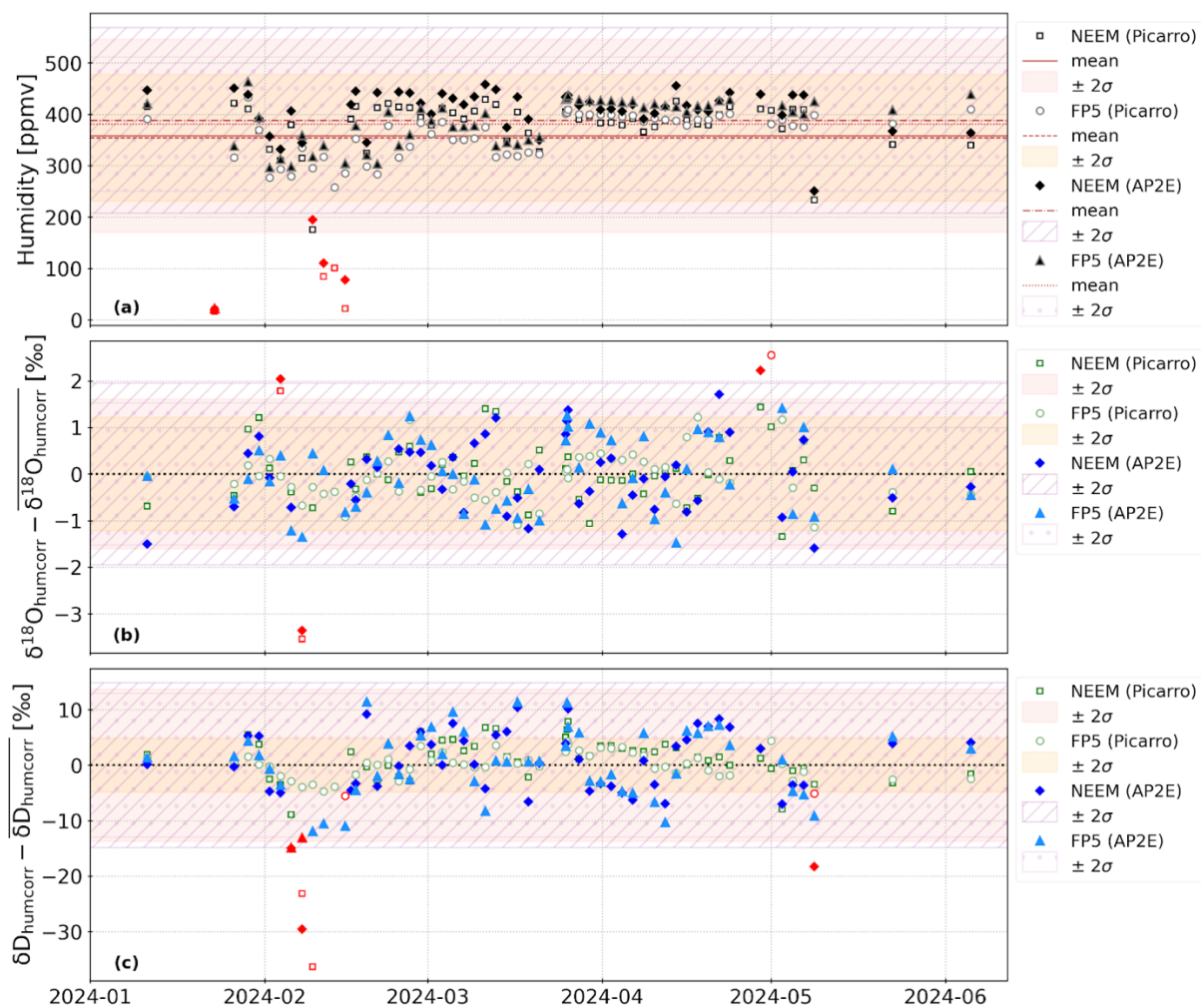
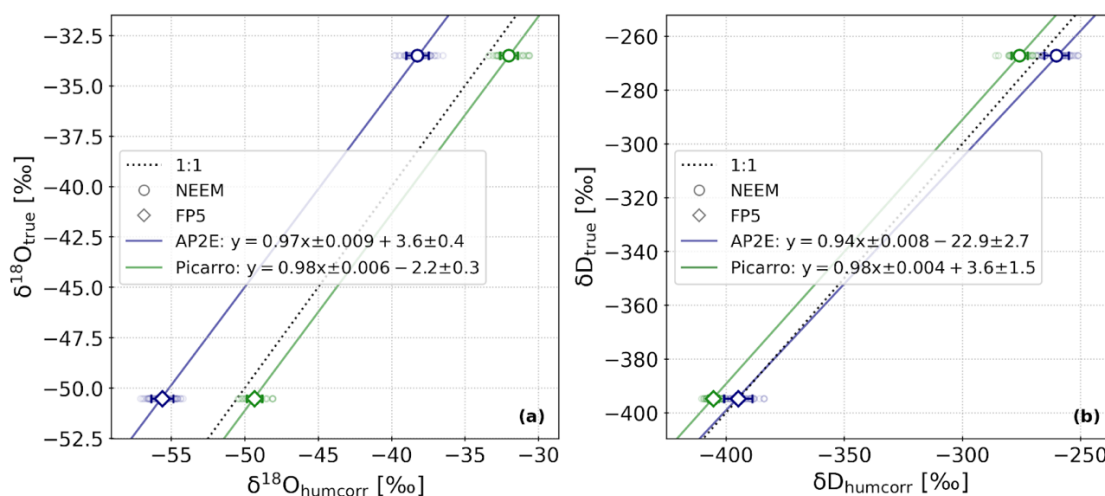


Figure 4: Results of the regular calibrations performed with two laboratory standards (FP5 and NEEM) between January 11th and June 6th with the new version of the LHLG (description in Sect. 2.2.2 and 2.2.3). Panel (a) shows the humidity measured by both analysers during each calibration. The red markers show the calibrations that were discarded (outside of two standard deviations around the mean humidity). Panels (b) and (c) show the measured isotopic ratios by both analysers during each calibration as a deviation to the mean over the whole period. The isotopic ratios of each calibration are corrected for the isotope-humidity response of each analyser. In panels (b) and (c), only the accepted calibration from panel (a) are shown. The red markers show the calibrations that are discarded in a second step (outside of two standard deviations around the mean isotopic ratio).

350

355

As described in Sect. 2.2.3, the results of the regular calibrations over six months are used to calibrate the data against the VSMOW-SLAP scale (selected calibrations from Fig. 4). Figure 5 shows the result of the linear regressions between the true and humidity-corrected $\delta^{18}\text{O}$ and δD . The coefficients of the linear regressions (used in Eq. 3) for both analysers and both isotope species are summarised in Table 3.



360

Figure 5: Humidity-isotope corrected ratios vs true isotopic ratios ($\delta^{18}\text{O}$ in panel (a) and δD in panel (b)) of two laboratory standards (FP5 and NEEM) for both Picarro and AP2E analysers. In both panels, the smaller coloured markers represent all selected calibrations and the larger coloured markers represent the average isotopic ratio of all selected calibrations (whiskers represent one standard deviation). The coloured lines show the linear regressions between the true and humidity-corrected isotopic ratios using two laboratory standards.

365

Table 3. Coefficients from the linear regressions between the true and humidity-corrected isotopic ratios using two laboratory standards (shown in Fig. 5 and used in Eq. 3) to calibrate the data from both Picarro and AP2E analysers against VSMOW-SLAP. The uncertainty associated with each coefficient corresponds to the standard error of the estimated coefficient (given by the *linregress* function from the python package *scipy*).

370

	$\delta^{18}\text{O}$		δD	
	Slope _{VSMOW-SLAP} [‰ ‰ ⁻¹]	Int _{VSMOW-SLAP} [‰]	Slope _{VSMOW-SLAP} [‰ ‰ ⁻¹]	Int _{VSMOW-SLAP} [‰]
Picarro HIDS2308	0.98 ± 0.006	-2.2 ± 0.3	0.98 ± 0.004	3.6 ± 1.5
AP2E	0.97 ± 0.009	3.6 ± 0.4	0.94 ± 0.008	-22.9 ± 2.7

Both the Picarro and AP2E analysers have an absolute calibration slope for $\delta^{18}\text{O}$ close to one (respectively 0.98 and 0.97, Fig. 5a and Table 3), which shows that both analysers capture the linearity between the true $\delta^{18}\text{O}$ value of the two laboratory standards. The intercepts of the linear relations for the two analysers are of the same magnitude, however opposite signs (-2.2‰ for Picarro and 3.6‰ for AP2E, Fig. 5a and Table 3). This indicates that the absolute calibration of the AP2E analyser will be of opposite sign and slightly larger than the Picarro, which is also visible in Fig. 6 and 7. The associated error on both linear coefficients from the two analysers are also comparable, despite the ones for the AP2E analyser being slightly higher (Fig. 5a and Table 3).

375

For δD , the Picarro shows an absolute calibration slope also close to one (0.98), while the AP2E analyser shows a lower slope (0.94, Fig. 5b and Table 3). This indicates that the Picarro also captures the linearity of the true δD value of the two laboratory standards, while the AP2E requires a stronger correction to calibrate the data against VSMOW-SLAP. Similarly, the intercepts of the linear relations are very different and of opposite signs between the two analysers (3.6‰ for Picarro and

380



385 -22.9‰ for AP2E, Fig. 5a and Table 3). This shows that the AP2E analyser is measuring further away than the true isotopic composition compared to the Picarro, and therefore that the correction to calibrate the AP2E analyser will be stronger than the one for the Picarro. This is also visible in Fig. 6 and 7. The results of the linear regressions for δD also show that the errors associated to the coefficients for the AP2E analyser are twice as high than the ones for the Picarro (Fig. 5 and Table 3). This means that the error on the absolute calibration of the AP2E analyser is higher, as also described in the following section (Sect. 3.1.4).

390 3.1.4 Measurement uncertainty

In Eq. 4 (Sect. 2.2.4), $\sigma_{i,drift}$ is estimated as one standard deviation of the selected calibrations over six months, combining both laboratory standards (Fig. 4b and c). Table 4 summarises the values of $\sigma_{i,drift}$ found for $\delta^{18}O$ and δD and for each analyser. Associated with the measured atmospheric humidity, this provides the measurement uncertainty on the final $\delta^{18}O$, δD and d-excess from both analysers presented along the data in the following section.

395

Table 4. Values of $\sigma_{i,drift}$ from Eq. 4 in Sect. 2.2.4 for both $\delta^{18}O$ and δD and both laser spectrometers.

	σ_{drift} for $\delta^{18}O$ [‰]	σ_{drift} for δD [‰]
Picarro HIDS2308	0.6	2.9
AP2E	0.8	5.6

400

Besides, the Monte Carlo tests show that between December 2023 and January 2024, the uncertainty (σ_{MC}) of $\delta^{18}O$ from the Picarro is 0.5‰ and 2.7‰ for δD , which leads to an uncertainty of 3.0‰ on d-excess. The AP2E analyser shows higher uncertainties, with $\sigma_{MC} = 0.8‰$ for $\delta^{18}O$, 4.9‰ for δD , and 5.3‰ for d-excess. As expected, the errors σ_{MC} on $\delta^{18}O$ and δD are in the same order of magnitude as the corresponding σ_{drift} (Table 4), since they are computed with the same set of calibrations (Sect. 2.2.4).

405

3.2 Time series of the water vapor isotopic composition

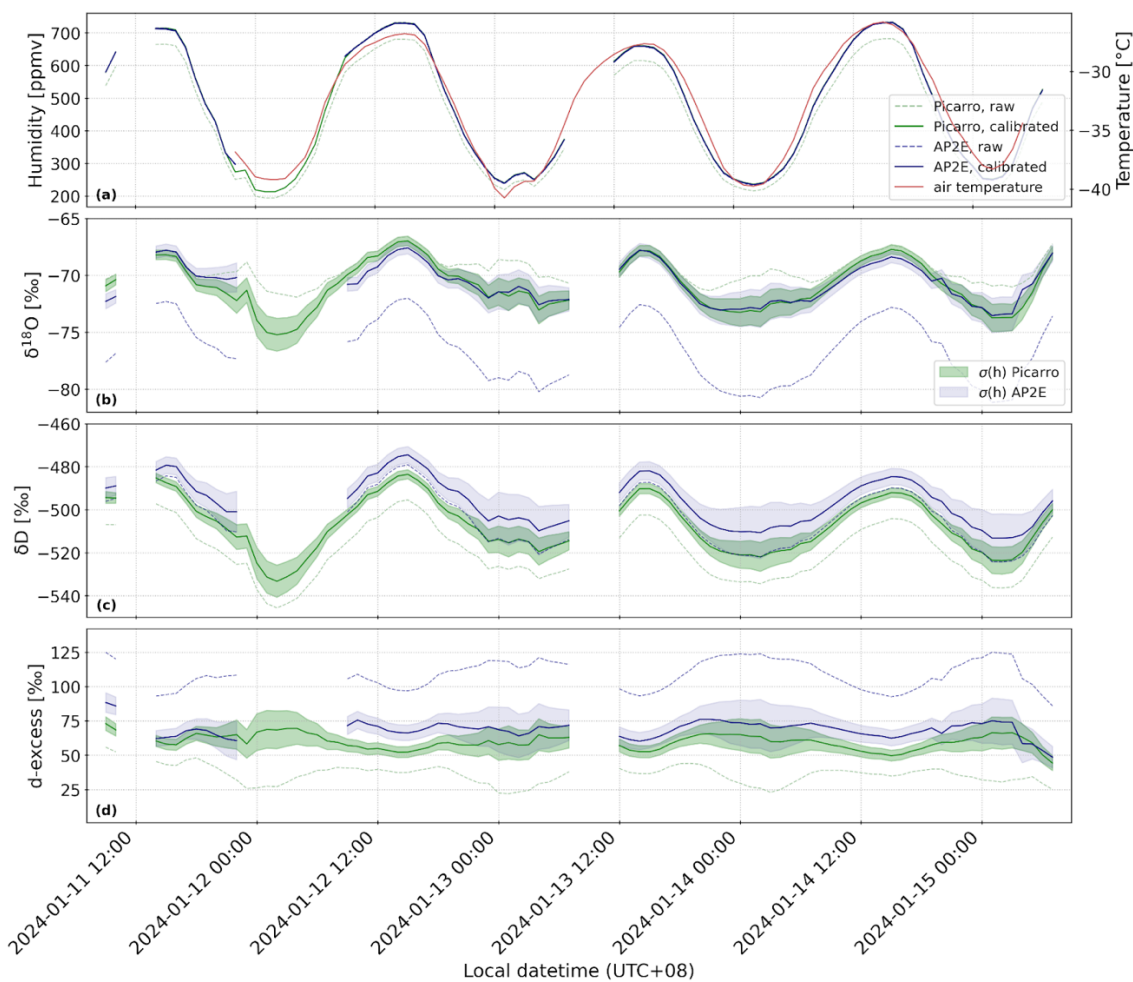
Figure 6 shows the evolution of the atmospheric humidity, $\delta^{18}O$, δD and d-excess measured by both laser spectrometers between December 2023 and March 15th 2024. Figure 7 shows a focus on a four-day period in January 2024 (corresponding to the grey hatched area in Fig. 6). Note that the time series are not continuous, with interruptions due to calibration periods, maintenance work on the instruments or electrical shutdowns.

410



415

Figure 6: Time series (December 6th 2023 to March 15th 2024) of the atmospheric humidity (in ppmv, panel (a)), $\delta^{18}\text{O}$ (in ‰, panel (b)), δD (in ‰, panel (c)) and d-excess (in ‰, panel (d)) measured by the Picarro (green lines) and AP2E (blue lines) analysers. In panels (b), (c) and (d), the green and blue shaded areas correspond respectively to $\sigma(h)$ (Sect. 2.2.4) of the Picarro and AP2E analysers. In all four panels, the dashed lines correspond to the raw data given by the spectrometers and the plain lines correspond to the corrected and calibrated data (see Sect. 2.2 and 3.1). The grey hatched area marks the period from January 11th to January 15th shown in Fig. 7.



420

425

Figure 7: Zoom on the period from January 11th to January 15th 2024 of the atmospheric humidity (in ppmv, panel (a)), $\delta^{18}\text{O}$ (in ‰, panel (b)), δD (in ‰, panel (c)) and d-excess (in ‰, panel (d)) measured by the Picarro (green lines) and AP2E (blue lines) analysers. In panels (b), (c) and (d), the green and blue shaded areas correspond respectively to $\sigma(h)$ (Sect. 2.2.4) of the Picarro and AP2E analysers. In all four panels, the dashed lines correspond to the raw data given by the spectrometers and the plain lines correspond to the corrected and calibrated data (see Sect. 2.2 and 3.1). In panel (a), the red line corresponds to the observed air temperature.

The raw humidity measured by both analysers are in excellent agreement (Fig. 6 and 7), and the calibration against the independent humidity sensor has only a small effect. The calibrated humidities are showing the same diurnal variations for both analysers, synchronous with the temperature diurnal cycle on site (Fig. 7a). In addition, both instruments record the decrease of the humidity from the beginning of February, coinciding with the onset of the winter at Dome C (Fig. 6a).

Contrary to the humidity, the calibration of the raw data has a significant effect on the $\delta^{18}\text{O}$ time series of both analysers. For the AP2E analyser, the calibration of the raw $\delta^{18}\text{O}$ time series shifts it towards higher values (Fig. 6 and 7), with a mean difference of 6‰ over December and January between the raw and calibrated time series. This shift is expected from the



435 absolute calibration curve (Sect. 3.1.3). The amplitude of the diurnal cycle is also slightly reduced after applying the
calibration (Fig. 7), due to the humidity- $\delta^{18}\text{O}$ response of the analyser (i.e. positive correction for low humidities and
negative correction for high humidities, Sect. 3.1.2). For the Picarro analyser, no systematic shift is observed before and after
the calibration of $\delta^{18}\text{O}$ (Fig. 6 and 7). However, the amplitude of the diurnal cycle is larger after calibration, as expected
from the humidity- $\delta^{18}\text{O}$ response of the Picarro which shows negative correction for lower humidities (Fig. 3, Sect. 3.1.2).
440 This is further visible on the period from the end of January onwards, where the diurnal cycles show an opposite behaviour
between the raw and calibrated data: the raw data is in opposite phase to the humidity (minimum $\delta^{18}\text{O}$ associated with
maximum humidity) and the calibrated data is in phase with the humidity (minimum $\delta^{18}\text{O}$ associated with minimum
humidity). This is an effect of the large humidity- $\delta^{18}\text{O}$ response of the Picarro at low humidities (Fig. 3, Sect. 3.1.2).
Compared to $\delta^{18}\text{O}$, the raw and calibrated δD time series from both instruments are rather similar, at least during the period
445 where the humidity is above 200 ppmv (mid-December to end of January, Fig. 6c). The calibration of both analysers slightly
increases the average δD values (+7‰ for the AP2E analyser and +12‰ for the Picarro analyser on average over December
and January). The calibration of the δD time series does not affect the amplitude of the diurnal cycle for neither analyser
(Fig. 7c). Both raw δD time series compare relatively well from mid-December to the end of January (dashed lines in Fig.
6c), with the same in-phase relationship between δD and the mixing ratio as for the calibrated $\delta^{18}\text{O}$ time series. This in-phase
450 relationship between δD and the humidity is preserved after calibration (plain lines in Fig. 6c and 7c).

There is a good agreement between the $\delta^{18}\text{O}$ calibrated time series from the AP2E and Picarro analysers between mid-
December to mid-February, confirming that the calibration is valid for the range of humidities encountered over this period.
The mean difference in $\delta^{18}\text{O}$ between the two instruments over the same period is 2‰, within the range of uncertainties of
455 the calibrated time series (Fig. 6). After mid-February, with humidity levels consistently below 200 ppmv (Fig. 6a), there is
an increasing difference between the AP2E and Picarro analysers (Fig. 6).

As for $\delta^{18}\text{O}$, we observe that the calibrated δD time series from both instruments agree well between mid-December to mid-
February (Fig. 6). There is a mean difference in δD between the two instruments of 8‰ over this period, which is also within
the uncertainty of both calibrated time series (Fig. 6 and 7). Similarly to $\delta^{18}\text{O}$, we observe that after mid-February, the
460 calibrated δD time series of the two instruments start to diverge (Fig. 6).

Finally, the raw time series of d-excess are very different between the two analysers (Fig. 6 and 7). However, after the
calibration of both analysers, the two d-excess time series are comparable within their uncertainty range (Fig. 6 and 7), with
a mean difference between the two analysers of 7‰ between mid-December and mid-February. As for $\delta^{18}\text{O}$ and δD , the
calibrated d-excess time series of the two analysers diverge from mid-February onwards (plain lines in Fig. 6d).

465 The divergence in both $\delta^{18}\text{O}$ and δD between the two instruments is probably due to the increase of instantaneous
measurement noise of the analysers when the humidity decreases. It is also related to the difficulty of calibrating the
instruments for very low humidity levels (Sect. 3.1.2). This is reflected in the uncertainty of the measurements (Fig. 6 and 7),



470 which increases significantly for both instruments from mid-February onwards, when the mixing ratio is consistently below 200 ppmv (Fig. 6). Because of these limitations, the comparison between the observations and the model presented in Sect. 3.3 is restricted to the period before mid-February.

475 In addition, the amplitude of the mean diurnal cycle in $\delta^{18}\text{O}$ (calibrated data, calculated over the period January 11th to January 15th 2024 shown in Fig. 7b) is similar for both instruments: 5.7‰ for the Picarro analyser (from -73.4 to -67.7‰, not shown) and 4.7‰ for the AP2E analyser (from -72.6 to 67.9‰, not shown). The mean diurnal cycle in δD over the same period is also comparable for both analysers: 34.9‰ for the Picarro analyser (from -523.2 to -488.3‰, not shown) and 29.5‰ for the AP2E analyser (from -509.6 to -480.1‰, not shown). As for $\delta^{18}\text{O}$ and δD , both instruments show a similar mean diurnal cycle in d-excess: 11.6‰ (from 52.9 to 64.5‰, not shown) for the Picarro analyser and 13.5‰ (from 63.2 to 76.7‰, not shown) for the AP2E analyser. Considering the uncertainties on the $\delta^{18}\text{O}$, δD and d-excess values of both instruments, we conclude that both analysers compare well and that the AP2E captures well the diurnal cycle measured by
480 the Picarro analyser.

3.3 Comparison of LMDZ6-iso outputs with novel in-situ measurements

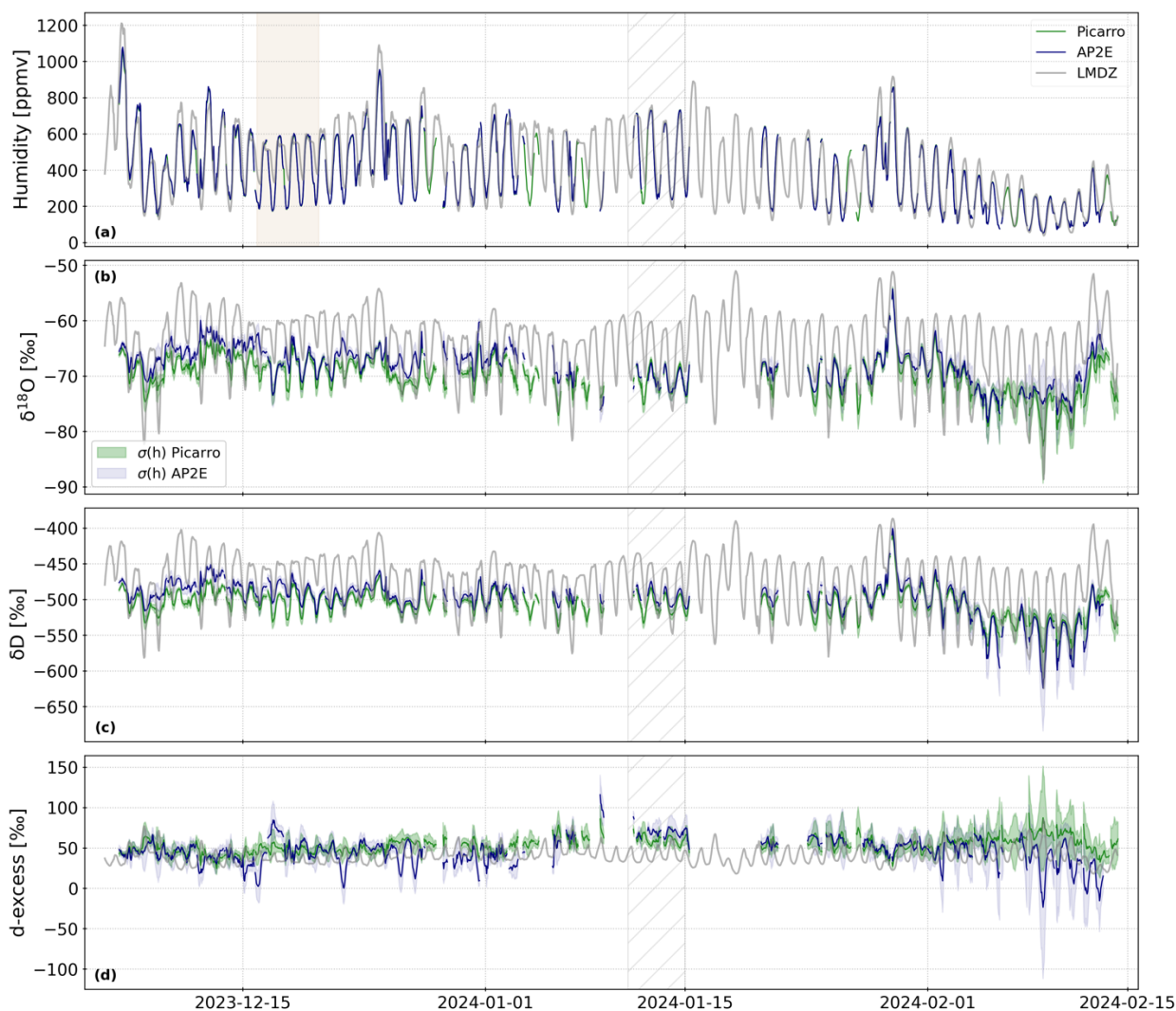
485 Recently, Dutrievoz et al. (*in review*) used in-situ observations of the water vapour isotopic composition at Concordia Station to evaluate the performance of LMDZ6-iso to correctly capture the diurnal variations observed on site. This comparison was performed over December 2018 and limited to $\delta^{18}\text{O}$ due to the low confidence in the d-excess measurements. Because of the large correction linked to the humidity-dependence on the $\delta^{18}\text{O}$ signal, even the $\delta^{18}\text{O}$ could be challenged. We extend this comparison to the recent period December 2023 to mid-February 2024 using the novel and reliable dataset presented in Sect. 3.2. Figure 8 shows the comparison of the humidity, $\delta^{18}\text{O}$, δD and d-excess over the whole period. Figure 9 shows the same for a four-day period in January 2024 (corresponding to the grey hatched area in Fig. 8).

490 The comparison of the humidity modelled by LMDZ6-iso and measured by both analysers show an overall good agreement, including for the amplitude of the observed diurnal cycle (Fig. 8a and 9a). However, during some specific periods, the model shows higher humidity levels than what is observed, especially during the nighttime (e.g. December 16th to 20th, light brown area in Fig. 8a).

495 Although the model reproduces the observed in-phase relationship between $\delta^{18}\text{O}$ and the humidity, the comparison between the modelled and observed $\delta^{18}\text{O}$ shows a poorer agreement than for humidity. Firstly, the modelled $\delta^{18}\text{O}$ shows an overall positive bias during the period December to mid-February compared to the observations, with a mean difference of 5.2‰ compared to the Picarro analyser and 3.3‰ compared to the AP2E analyser (Fig. 8b). Secondly, the amplitude of the diurnal cycle modelled by LMDZ6-iso is overall larger than in the observations (Fig. 8b). Over the period January 11th to January 15th 2024 (Fig. 9b), the amplitude of the mean diurnal cycle in $\delta^{18}\text{O}$ modelled by LMDZ6-iso is 10.9‰ (from -70.9 to -



500 60.0‰, not shown), higher than the one from both the Picarro analyser (5.7‰, Sect. 3.2) and the AP2E analyser (4.7‰, Sect. 3.2).



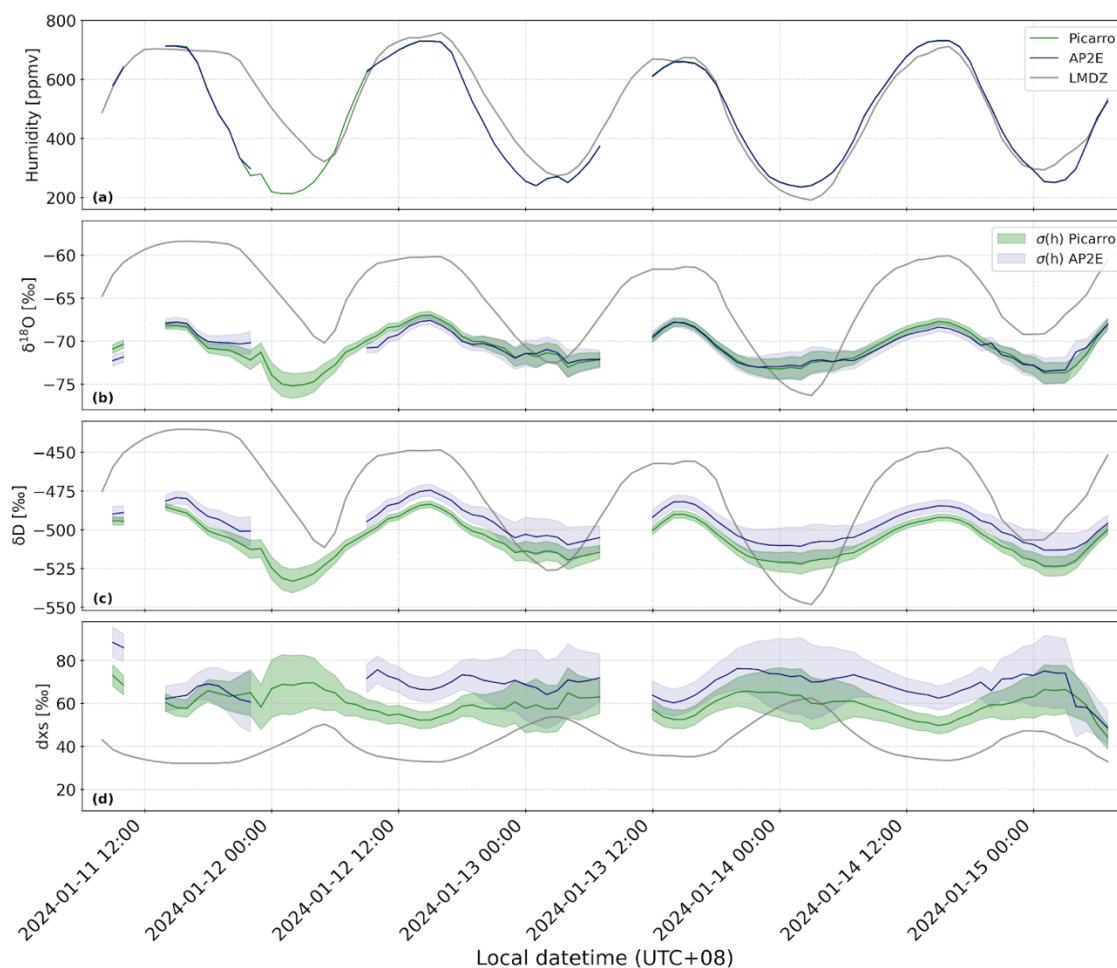
505 **Figure 8:** Time series (December 5th 2023 to February 14th 2024) of the atmospheric humidity (in ppmv, panel (a)), $\delta^{18}\text{O}$ (in ‰, panel (b)), δD (in ‰, panel (c)), and d-excess (in ‰, panel (d)) measured (and calibrated) by the Picarro analyser (green lines), the AP2E (blue lines) analysers, and modelled by LMDZ6-iso (grey lines). In panels (b), (c) and (d), the green and blue shaded areas correspond respectively to $\sigma(h)$ (Sect. 2.2.4) of the Picarro and AP2E analysers. In all four panels, the grey hatched area marks the period from January 1st to 11th 2024 shown in Fig. 9 (same period as in Fig. 7). In panel (a), the light brown area marks the period from December 16th to 20th 2023 (period when the modelled and observed humidities differ).

510 The same patterns are observed for δD . The modelled δD also shows an overall mean positive bias compared to the observations, with a mean difference of 28.9‰ compared to the Picarro analyser and 20.9‰ compared to the AP2E analyser (Fig. 8c). The amplitude of the diurnal cycle is also larger in LMDZ6-iso than in the observations (Fig. 8c). Between January



11th and January 15th 2024 (Fig. 9c), the mean diurnal amplitude modelled by LMDZ6-iso is 69.0‰ (from -515.8 to -
515 446.8‰, not shown), which is higher than the observed one (34.9‰ for Picarro analyser, 29.5‰ for AP2E analyser, Sect.
3.2).

Lastly, due to the biases identified for $\delta^{18}\text{O}$ and δD , the d-excess modelled by LMDZ6-iso also shows some discrepancies
with the observations. The model shows an overall negative bias compared to the observations, with a mean difference
between December and mid-February of 12.5‰ compared to the Picarro analyser and of 5.1‰ compared to the AP2E
520 analyser (Fig. 8d). The comparison of the amplitudes of the diurnal cycle is less conclusive than for $\delta^{18}\text{O}$ and δD , due to the
large uncertainties associated with the observations (Fig. 9d). However, we observe that the model still correctly captures the
observed anti-phase relationship between d-excess and $\delta^{18}\text{O}$ (or δD), with a maximum d-excess when $\delta^{18}\text{O}$ is minimal, i.e.
during the night, and a minimum d-excess when $\delta^{18}\text{O}$ is maximal, i.e. during the day (Fig. 9d).



525

Figure 9: Zoom on the period from January 11th to 15th 2024 of the atmospheric humidity (in ppmv, panel (a)), $\delta^{18}\text{O}$ (in ‰, panel (b)), δD (in ‰, panel (c)) and d-excess (in ‰, panel (d)) measured by the Picarro analyser (green lines), the AP2E analyser (blue



lines), and modelled by LMDZ6-iso (grey lines). In panels (b) to (d), the green and blue shaded areas correspond respectively to $\sigma(h)$ (Sect. 2.2.4) of the Picarro and AP2E analysers.

530

Although the aim of this study is not to provide an in-depth evaluation of the LMDZ6-iso model, the discrepancies observed between the outputs of the model and the observations can provide indications on the possible biases in the model. This is discussed in the following section.

4 Discussion

535 We show that over the period from December 5th 2023 to January 31st 2024, there is a good agreement between the calibrated humidity, $\delta^{18}\text{O}$ and δD time series from the AP2E and Picarro water vapour analysers. We therefore use this new dataset as the best measurements documenting the diurnal variability of water vapour isotopic composition during the summertime at Concordia Station. It permits to evaluate the humidity, $\delta^{18}\text{O}$ and δD modelled by LMDZ6-iso for the lowest atmospheric level (0-7 m above the surface at Dome C). In general, there is a good agreement between the modelled and
540 observed humidity. The model also captures the observed evolution of the diurnal cycles of the water vapour isotopic composition. However, the model shows both a mean bias in the water vapour isotopic composition and a discrepancy in the amplitude of the daily cycle compared to the observations.

Our results support the conclusions from Dutrievoz et al. (*in review*), who showed larger amplitudes of the modelled $\delta^{18}\text{O}$
545 and δD diurnal cycles in the model compared to observations. Dutrievoz et al. (*in review*) suggested that one explanation for this discrepancy could be that the model doesn't include the process of fractionation during sublimation, which has been shown to occur (Wahl et al., 2021). Sublimation generally enriches the snow surface in $\delta^{18}\text{O}$ and δD (Casado et al., 2021; Hughes et al., 2021; Dietrich et al., 2023), which would lead to a decrease in the vapour $\delta^{18}\text{O}$ and δD during the day (i.e. when sublimation occurs, coincides with higher humidity, $\delta^{18}\text{O}$ and δD levels). Including fractionation during sublimation
550 could probably improve the comparison between the modelled and observed diurnal cycle of the water vapour isotopic composition. The discrepancy between the model and the observations could also arise from the ice-vapour equilibrium fractionation coefficients used in LMDZ6-iso (Sect. 2.3). These coefficients were established for temperatures down to -40 and -33°C, respectively, and extrapolated for lower temperatures. In addition, other fractionation coefficients from the literature disagree with the formulations from Merlivat and Nief (1967) and Majoube (1971a) (Ellehoj et al., 2013; Lamb et al., 2017). Lastly, the amplitude of the water vapour isotopic composition diurnal cycle is also controlled by the amount of
555 sublimation and turbulent mixing in the boundary layer during the day, and by condensation during the night. Although included in the model, these processes might not be well representing the in-situ conditions.

We also observe that mean values of both $\delta^{18}\text{O}$ and δD in the water vapour are higher in LMDZ6-iso than in the
560 observations. On the other hand, the modelled vapour d-excess is, on average, lower than in the observations. The bias in the



565 modelled $\delta^{18}\text{O}$ and δD was also identified by Dutrievoz et al. (*in review*), despite the high uncertainty associated with the measurements. This overall bias in the modelled vapour isotopic composition could be explained by the isotopic composition of the snow in LMDZ6-iso, which might differ significantly from the actual snow surface at Dome C. Indeed, the snow isotopic composition in LMDZ6-iso during December 2023 and January 2024 is higher (+1‰ in $\delta^{18}\text{O}$ and +19‰ in δD) than the observed mean isotopic composition of the snow surface in December and January (average over the period 2017-2021, Ollivier et al. 2024).

570 The water vapour isotopic measurements presented in this study provide important benchmarks to evaluate the performance of isoAGCMs. The discrepancies identified between LMDZ6-iso and the observations highlight issues in the model physics and/or in the implementation of water isotopes in the model. Combining the observations of the water vapour isotopic composition with other meteorological observations brings new constraints to improve the representation of the Antarctic boundary layer in models and to reduce the uncertainty on isotopic fractionation coefficients at low temperatures. Both are needed to improve isoAGCMs in Antarctica, which in turn are needed for a better climatic interpretation of isotope records from Antarctic ice cores.

575 **5 Data availability**

Data described in this manuscript can be accessed at Zenodo under <https://doi.org/10.5281/zenodo.14569655> (Landais et al., 2024b).

6 Conclusions

580 We have installed at Concordia Station two water vapour isotopic analysers using different optical spectroscopy techniques and optimised for measuring at low humidities. The two instruments were carefully and independently calibrated with a dedicated calibration unit designed to generate low humidity levels. This permitted accurate measurements of the atmospheric water vapour isotopic composition at Concordia Station for a 2.5-month long period during the austral summer 2023-2024 and to validate the performance of the OF-CEAS measurement technique against CRDS for in-situ measurements. In addition, the thorough calibration of the instruments permitted to constrain the uncertainty on the datasets, 585 which can be used to evaluate isotope-enabled atmospheric general circulation models.

As a demonstration of the usefulness of the new dataset, we used this novel dataset to compare with the outputs from LMDZ6-iso, which shows two types of biases in the model outputs. The model first shows a mean bias of the water vapour isotopic composition over the study period (positive bias in $\delta^{18}\text{O}$ and δD , negative bias in d-excess). In addition, the model



590 overestimates the amplitude of the diurnal cycle in the water vapour $\delta^{18}\text{O}$ and δD . This confirms the model-observations discrepancies identified by Dutrievoz et al. (*in review*).

The instruments installed at Concordia Station will continue to record the atmospheric water vapour isotopic composition in the upcoming years, to complement ongoing isotopic measurements of precipitation and snow (Dreossi et al., 2024; Ollivier et al., 2024) and to provide long-term measurements at this remote location on the East Antarctic Plateau. Further improvements are still needed to reduce the measurement uncertainties and to constrain the humidity-isotope calibration 595 curves down to very low humidities (below 100 ppmv) to be able to measure during the wintertime. This will be done by improving the accuracy of the calibration at very low humidity levels (e.g. by reducing the effect of residual water mixing effects) and through the development of a new generation of laser spectrometers (Casado et al., 2024).

Author contribution. IO, TL and AL designed the study and contributed to the analysis. IO and TL performed the data 600 curation and formal analysis, and IO performed the visualisation. IO, TL, MC, EF, OJ, FP and AL participated to the acquisition of the water vapor isotopic data. TL performed the field calibration and optimisation of the instruments. ND and CA performed the model simulations and provided inputs to the study. CG acquired the meteorological data and provided inputs to the study. HCSL provided inputs to the calibration protocol and data uncertainty estimation. IO, TL and AL prepared the manuscript draft, and all authors contributed to reviews and edits.

605 *Competing interests.* The authors declare that they have no conflict of interest.

Acknowledgments. This publication was generated in the frame of the DEEPICE and AWACA projects. The projects have received funding from the European Union's Horizon 2020 research and innovation programme under grant agreements no. 610 955750 (DEEPICE) and no. 951596 (AWACA). The water vapor isotopic data presented in this study has been collected within the frame of the French Polar Institute (IPEV) project NIVO 1110. We acknowledge using data from the project CALVA 1013 and GLACIOCLIM observatories supported by the French Polar Institute (IPEV) and the Observatoire des Sciences de l'Univers de Grenoble (OSUG) (<https://web.lmd.jussieu.fr/~cgenthon/SiteCALVA/CalvaData.html>, <https://glacioclim.osug.fr/>). We thank the logistics staff at Concordia Station and Manon Mastin for the instrumental 615 maintenance and help with the data acquisition.

References

Casado, M., Landais, A., Masson-Delmotte, V., Genthon, C., Kerstel, E., Kassi, S., Arnaud, L., Picard, G., Prie, F., Cattani, O., Steen-Larsen, H.-C., Vignon, E., and Cermak, P.: Continuous measurements of isotopic composition of water vapour on the EastAntarctic Plateau, *Atmos. Chem. Phys.*, 16, 8521–8538, <https://doi.org/10.5194/acp-16-8521-2016>, 2016.



- 620 Casado, M., Landais, A., Picard, G., Münch, T., Laepple, T., Stenni, B., Dreossi, G., Ekaykin, A., Arnaud, L., Genthon, C., Touzeau, A., Masson-Delmotte, V., and Jouzel, J.: Archival processes of the water stable isotope signal in East Antarctic ice cores, *The Cryosphere*, 12, 1745–1766, <https://doi.org/10.5194/tc-12-1745-2018>, 2018.
- Casado, M., Landais, A., Picard, G., Arnaud, L., Dreossi, G., Stenni, B., and Prié, F.: Water Isotopic Signature of Surface Snow Metamorphism in Antarctica, *Geophys Res Lett*, 48, <https://doi.org/10.1029/2021GL093382>, 2021.
- 625 Casado, M., Landais, A., Stoltmann, T., Chaillot, J., Daëron, M., Prié, F., Bordet, B., and Kassi, S.: Reliable water vapour isotopic composition measurements at low humidity using frequency-stabilised cavity ring-down spectroscopy, *Atmos. Meas. Tech.*, 17, 4599–4612, <https://doi.org/10.5194/amt-17-4599-2024>, 2024.
- Craig, H.: Standard for Reporting Concentrations of Deuterium and Oxygen-18 in Natural Waters, *Science*, 133, 1833–1834, <https://doi.org/10.1126/science.133.3467.1833>, 1961.
- 630 Dansgaard, W.: Stable isotopes in precipitation, *Tellus*, 16, 436–468, <https://doi.org/10.1111/j.2153-3490.1964.tb00181.x>, 1964.
- Dietrich, L. J., Steen-Larsen, H. C., Wahl, S., Jones, T. R., Town, M. S., and Werner, M.: Snow-Atmosphere Humidity Exchange at the Ice Sheet Surface Alters Annual Mean Climate Signals in Ice Core Records, *Geophysical Research Letters*, 50, e2023GL104249, <https://doi.org/10.1029/2023GL104249>, 2023.
- Dutrievoz, N., Agosta, C., Risi, C., Vignon, E., Nguyen, S., Landais, A., Fourné, E., Leroy-Dos Santos, C., Casado, M., Masson-Delmotte, V., Jouzel, J., Dubos, T., Ollivier, I., Stenni, B., Dreossi, G., Masiol, M., Minster, B., and Prié, F.: Antarctic water stable isotopes in the global atmospheric model LMDZ6: from climatology to boundary layer processes, *in review in JGR Atmospheres*.
- 635 Ellehoj, M. D., Steen-Larsen, H. C., Johnsen, S. J., and Madsen, M. B.: Ice-vapor equilibrium fractionation factor of hydrogen and oxygen isotopes: Experimental investigations and implications for stable water isotope studies, *Rapid Comm Mass Spectrometry*, 27, 2149–2158, <https://doi.org/10.1002/rcm.6668>, 2013.
- 640 Eyring, V., Bony, S., Meehl, G. A., Senior, C. A., Stevens, B., Stouffer, R. J., and Taylor, K. E.: Overview of the Coupled Model Intercomparison Project Phase 6 (CMIP6) experimental design and organization, *Geosci. Model Dev.*, 9, 1937–1958, <https://doi.org/10.5194/gmd-9-1937-2016>, 2016.
- Genthon, C., Piard, L., Vignon, E., Madeleine, J.-B., Casado, M., and Gallée, H.: Atmospheric moisture supersaturation in the near-surface atmosphere at Dome C, Antarctic Plateau, *Atmos. Chem. Phys.*, 17, 691–704, <https://doi.org/10.5194/acp-17-691-2017>, 2017.
- 645 Genthon, C., Veron, D., Vignon, E., Six, D., Dufresne, J.-L., Madeleine, J.-B., Sultan, E., and Forget, F.: 10 years of temperature and wind observation on a 45 m tower at Dome C, East Antarctic plateau, *Earth Syst. Sci. Data*, 13, 5731–5746, <https://doi.org/10.5194/essd-13-5731-2021>, 2021.
- Genthon, C., Veron, D. E., Vignon, E., Madeleine, J.-B., and Piard, L.: Water vapor in cold and clean atmosphere: a 3-year data set in the boundary layer of Dome C, East Antarctic Plateau, *Earth Syst. Sci. Data*, 14, 1571–1580, <https://doi.org/10.5194/essd-14-1571-2022>, 2022.
- 650 Hourdin, F., Rio, C., Grandpeix, J., Madeleine, J., Cheruy, F., Rochetin, N., Jam, A., Musat, I., Idelkadi, A., Fairhead, L., Foujols, M., Mellul, L., Traore, A., Dufresne, J., Boucher, O., Lefebvre, M., Millour, E., Vignon, E., Jouhaud, J., Diallo, F. B., Lott, F., Gastineau, G., Caubel, A., Meurdesoif, Y., and Ghattas, J.: LMDZ6A: The Atmospheric Component of the IPSL Climate Model With Improved and Better Tuned Physics, *J Adv Model Earth Syst*, 12, e2019MS001892, <https://doi.org/10.1029/2019MS001892>, 2020.
- 655



- Hughes, A. G., Wahl, S., Jones, T. R., Zuhr, A., Hörhold, M., White, J. W. C., and Steen-Larsen, H. C.: The role of sublimation as a driver of climate signals in the water isotope content of surface snow: laboratory and field experimental results, *The Cryosphere*, 15, 4949–4974, <https://doi.org/10.5194/tc-15-4949-2021>, 2021.
- 660 Johnsen, S. J., Clausen, H. B., Dansgaard, W., Fuhrer, K., Gundestrup, N., Hammer, C. U., Iversen, P., Jouzel, J., Stauffer, B., and Steffensen, J. P.: Irregular glacial interstadials recorded in a new Greenland ice core, *Nature*, 359, 311–313, <https://doi.org/10.1038/359311a0>, 1992.
- Jouzel, J., and Merlivat, M.: Deuterium and oxygen 18 in precipitation: Modeling of the isotopic effects during snow formation, *J. Geophys. Res.*, 89, D7, 11749–11757, <https://doi.org/10.1029/JD089iD07p11749>, 1984.
- 665 Jouzel, J., Masson-Delmotte, V., Cattani, O., Dreyfus, G., Falourd, S., Hoffmann, G., Minster, B., Nouet, J., Barnola, J. M., Chappellaz, J., Fischer, H., Gallet, J. C., Johnsen, S., Leuenberger, M., Loulergue, L., Luethi, D., Oerter, H., Parrenin, F., Raisbeck, G., Raynaud, D., Schilt, A., Schwander, J., Selmo, E., Souchez, R., Spahni, R., Stauffer, B., Steffensen, J. P., Stenni, B., Stocker, T. F., Tison, J. L., Werner, M., and Wolff, E. W.: Orbital and Millennial Antarctic Climate Variability over the Past 800,000 Years, *Science*, 317, 793–796, <https://doi.org/10.1126/science.1141038>, 2007.
- 670 Lamb, K. D., Clouser, B. W., Bolot, M., Sarkozy, L., Ebert, V., Saathoff, H., Möhler, O., and Moyer, E. J.: Laboratory measurements of HDO/H₂O isotopic fractionation during ice deposition in simulated cirrus clouds, *Proc. Natl. Acad. Sci. U.S.A.*, 114, 5612–5617, <https://doi.org/10.1073/pnas.1618374114>, 2017.
- Landais, A., Stenni, B., Masson-Delmotte, V., Jouzel, J., Cauquoin, A., Fourré, E., Minster, B., Selmo, E., Extier, T., Werner, M., Vimeux, F., Uemura, R., Crotti, I., and Grisart, A.: Interglacial Antarctic–Southern Ocean climate decoupling due to moisture source area shifts, *Nat. Geosci.*, 14, 918–923, <https://doi.org/10.1038/s41561-021-00856-4>, 2021.
- 675 Landais, A., Agosta, C., Vimeux, F., Magand, O., Solis, C., Cauquoin, A., Dutrievoz, N., Risi, C., Leroy-Dos Santos, C., Fourré, E., Cattani, O., Jossoud, O., Minster, B., Prié, F., Casado, M., Dommergue, A., Bertrand, Y., and Werner, M.: Abrupt excursions in water vapor isotopic variability at the Pointe Benedicte observatory on Amsterdam Island, *Atmos. Chem. Phys.*, 24, 4611–4634, <https://doi.org/10.5194/acp-24-4611-2024>, 2024a.
- 680 Landais, A., Ollivier, I., Lauwers, T., and Jossoud, O.: Isotopic composition of the atmospheric water vapor during the austral summer at Concordia Station, Dome C, East Antarctica (December 2023 – February 2024), Zenodo [dataset], <https://doi.org/10.5281/zenodo.14569655>, 2024b.
- Lauwers, T., Fourré, E., Jossoud, O., Romanini, D., Prié, F., Nitti, G., Casado, M., Jaulin, K., Miltner, M., Farradèche, M., Masson-Delmotte, V., and Landais, A.: OF-CEAS laser spectroscopy to measure water isotopes in dry environments: example of application in Antarctica, <https://doi.org/10.5194/egusphere-2024-2149>, 15 August 2024.
- 685 Leroy-Dos Santos, C., Casado, M., Prié, F., Jossoud, O., Kerstel, E., Farradèche, M., Kassi, S., Fourré, E., and Landais, A.: A dedicated robust instrument for water vapor generation at low humidity for use with a laser water isotope analyzer in cold and dry polar regions, *Atmos. Meas. Tech.*, 14, 2907–2918, <https://doi.org/10.5194/amt-14-2907-2021>, 2021.
- Leroy-Dos Santos, C., Fourré, E., Agosta, C., Casado, M., Cauquoin, A., Werner, M., Minster, B., Prié, F., Jossoud, O., Petit, L., and Landais, A.: From atmospheric water isotopes measurement to firn core interpretation in Adélie Land: a case study for isotope-enabled atmospheric models in Antarctica, *The Cryosphere*, 17, 5241–5254, <https://doi.org/10.5194/tc-17-5241-2023>, 2023.
- 690 Lorius, C., Merlivat, L., Jouzel, J., and Pourchet, M.: A 30,000-yr isotope climatic record from Antarctic ice, *Nature*, 280, 644–648, <https://doi.org/10.1038/280644a0>, 1979.



- 695 Madsen, M. V., Steen-Larsen, H. C., Hörhold, M., Box, J., Berben, S. M. P., Capron, E., Faber, A. -K., Hubbard, A., Jensen, M. F., Jones, T. R., Kipfstuhl, S., Koldtoft, I., Pillar, H. R., Vaughn, B. H., Vladimirova, D., and Dahl-Jensen, D.: Evidence of Isotopic Fractionation During Vapor Exchange Between the Atmosphere and the Snow Surface in Greenland, *J. Geophys. Res. Atmos.*, 124, 2932–2945, <https://doi.org/10.1029/2018JD029619>, 2019.
- Majoube, M.: Fractionnement en ^{18}O entre la glace et la vapeur d'eau, *J. Chim. Phys. Phys. Chim. Biol.*, 68, 625–636, <https://doi.org/10.1051/jcp/1971680625>, 1971a.
- 700 Majoube, M.: Fractionnement en Oxygène 18 et en Deutérium entre l'eau et sa vapeur, *J. Chim. Phys. Phys. Chim. Biol.*, 10, 1423–1436, <https://doi.org/10.1051/jcp/1971681423>, 1971b.
- Merlivat, L. and Jouzel, J.: Global climatic interpretation of the deuterium-oxygen 18 relationship for precipitation, *J. Geophys. Res.*, 84, 5029–5033, <https://doi.org/10.1029/JC084iC08p05029>, 1979.
- Merlivat, L. and Nief, G.: Fractionnement isotopique lors des changements d'état solide-vapeur et liquide-vapeur de l'eau à des températures inférieures à 0°C , *Tellus*, 19, 122–127, <https://doi.org/10.1111/j.2153-3490.1967.tb01465.x>, 1967.
- 705 Murphy, D. M. and Koop, T.: Review of the vapour pressures of ice and supercooled water for atmospheric applications, *Q. J. R. Meteorol. Soc.*, 131, 1539–1565, <https://doi.org/10.1256/qj.04.94>, 2005.
- Ollivier, I., Steen-Larsen, H. C., Stenni, B., Arnaud, L., Casado, M., Cauquoin, A., Dreossi, G., Genthon, C., Minster, B., Picard, G., Werner, M., and Landais, A.: Surface processes and drivers of the snow water stable isotopic composition at Dome C, East Antarctica – a multi-dataset and modelling analysis, *The Cryosphere*, 19, 173–200, <https://doi.org/10.5194/tc-19-173-2025>, 2025.
- 710 Risi, C., Bony, S., Vimeux, F., and Jouzel, J.: Water-stable isotopes in the LMDZ4 general circulation model: Model evaluation for present-day and past climates and applications to climatic interpretations of tropical isotopic records, *J. Geophys. Res.*, 115, 2009JD013255, <https://doi.org/10.1029/2009JD013255>, 2010.
- Ritter, F., Steen-Larsen, H. C., Werner, M., Masson-Delmotte, V., Orsi, A., Behrens, M., Birnbaum, G., Freitag, J., Risi, C., and Kipfstuhl, S.: Isotopic exchange on the diurnal scale between near-surface snow and lower atmospheric water vapor at Kohlen station, East Antarctica, *The Cryosphere*, 10, 1647–1663, <https://doi.org/10.5194/tc-10-1647-2016>, 2016.
- 715 Steen-Larsen, H. C., Johnsen, S. J., Masson-Delmotte, V., Stenni, B., Risi, C., Sodemann, H., Balslev-Clausen, D., Blunier, T., Dahl-Jensen, D., Ellehøj, M. D., Falourd, S., Grindsted, A., Gkinis, V., Jouzel, J., Popp, T., Sheldon, S., Simonsen, S. B., Sjolte, J., Steffensen, J. P., Sperlich, P., Sveinbjörnsdóttir, A. E., Vinther, B. M., and White, J. W. C.: Continuous monitoring of summer surface water vapor isotopic composition above the Greenland Ice Sheet, *Atmos. Chem. Phys.*, 13, 4815–4828, <https://doi.org/10.5194/acp-13-4815-2013>, 2013.
- 720 Steen-Larsen, H. C., Masson-Delmotte, V., Hirabayashi, M., Winkler, R., Satow, K., Prié, F., Bayou, N., Brun, E., Cuffey, K. M., Dahl-Jensen, D., Dumont, M., Guillevic, M., Kipfstuhl, S., Landais, A., Popp, T., Risi, C., Steffen, K., Stenni, B., and Sveinbjörnsdóttir, A. E.: What controls the isotopic composition of Greenland surface snow?, *Clim. Past*, 10, 377–392, <https://doi.org/10.5194/cp-10-377-2014>, 2014.
- 725 Stenni, B., Masson-Delmotte, V., Selmo, E., Oerter, H., Meyer, H., Röthlisberger, R., Jouzel, J., Cattani, O., Falourd, S., Fischer, H., Hoffmann, G., Iacumin, P., Johnsen, S. J., Minster, B., and Udisti, R.: The deuterium excess records of EPICA Dome C and Dronning Maud Land ice cores (East Antarctica), *Quaternary Science Reviews*, 29, 146–159, <https://doi.org/10.1016/j.quascirev.2009.10.009>, 2010.



- 730 Town, M. S., Steen-Larsen, H. C., Wahl, S., Faber, A.-K., Behrens, M., Jones, T. R., and Sveinbjornsdottir, A.: Post-depositional modification on seasonal-to-interannual timescales alters the deuterium-excess signals in summer snow layers in Greenland, *The Cryosphere*, 18, 3653–3683, <https://doi.org/10.5194/tc-18-3653-2024>, 2024.
- Uemura, R., Matsui, Y., Yoshimura, K., Motoyama, H., and Yoshida, N.: Evidence of deuterium excess in water vapor as an indicator of ocean surface conditions, *J. Geophys. Res.*, 113, 2008JD010209, <https://doi.org/10.1029/2008JD010209>, 2008.
- 735 Van Leer, B.: Towards the ultimate conservative difference scheme. IV. A new approach to numerical convection, *Journal of Computational Physics*, 23, 276–299, [https://doi.org/10.1016/0021-9991\(77\)90095-X](https://doi.org/10.1016/0021-9991(77)90095-X), 1977.
- Vignon, É., Raillard, L., Genthon, C., Del Guasta, M., Heymsfield, A. J., Madeleine, J.-B., and Berne, A.: Ice fog observed at cirrus temperatures at Dome C, Antarctic Plateau, *Atmos. Chem. Phys.*, 22, 12857–12872, <https://doi.org/10.5194/acp-22-12857-2022>, 2022.
- 740 Vimeux, F., Masson, V., Jouzel, J., Stievenard, M., and Petit, J. R.: Glacial–interglacial changes in ocean surface conditions in the Southern Hemisphere, *Nature*, 398, 410–413, <https://doi.org/10.1038/18860>, 1999.
- Wahl, S., Steen-Larsen, H. C., Reuder, J., and Hörhold, M.: Quantifying the Stable Water Isotopologue Exchange Between the Snow Surface and Lower Atmosphere by Direct Flux Measurements, *Geophys Res Atmos*, 126, <https://doi.org/10.1029/2020JD034400>, 2021.
- 745 Wahl, S., Steen-Larsen, H. C., Hughes, A. G., Dietrich, L. J., Zuhr, A., Behrens, M., Faber, A. -K., and Hörhold, M.: Atmosphere-Snow Exchange Explains Surface Snow Isotope Variability, *Geophysical Research Letters*, 49, e2022GL099529, <https://doi.org/10.1029/2022GL099529>, 2022.
- Weng, Y., Touzeau, A., and Sodemann, H.: Correcting the impact of the isotope composition on the mixing ratio dependency of water vapour isotope measurements with cavity ring-down spectrometers, *Atmos. Meas. Tech.*, 13, 3167–3190, <https://doi.org/10.5194/amt-13-3167-2020>, 2020.
- 750 Werner, M., Langebroek, P. M., Carlsen, T., Herold, M., and Lohmann, G.: Stable water isotopes in the ECHAM5 general circulation model: Toward high-resolution isotope modeling on a global scale, *J. Geophys. Res.*, 116, D15109, <https://doi.org/10.1029/2011JD015681>, 2011.
- Zuhr, A. M., Wahl, S., Steen-Larsen, H. C., Hörhold, M., Meyer, H., and Laepple, T.: A Snapshot on the Buildup of the Stable Water Isotopic Signal in the Upper Snowpack at EastGRIP on the Greenland Ice Sheet, *JGR Earth Surface*, 128, e2022JF006767, <https://doi.org/10.1029/2022JF006767>, 2023.
- 755